The Meteoritical Society

Meteoritics & Planetary Science 57, Nr 4, 817–829 (2022)
doi: 10.1111/maps.13797

Sr distribution as proxy for Ca distribution at depth in SXRF analysis of mm-sized carbonaceous chondrites: Implications for asteroid sample return missions

B. J. TKALCEC*[1], P. TACK[2], E. DE PAUW[2], B. VEKEMANS[2], T. NAKAMURA[3], J. GARREVOET[4], G. FALKENBERG[4], L. VINCZE[2], and F. E. BRENKER[1]

[1]Department of Geosciences, Goethe University Frankfurt, Altenhoeferallee 1, Frankfurt am Main 60438, Germany
[2]Department of Chemistry, XMI Research Group, Ghent University, Krijgslaan 281 S12, Ghent 9000, Belgium
[3]Department of Earth Science, Tohoku University, Sendai, Miyagi 980-8578, Japan
[4]Deutsches Elektronen-Synchrotron DESY, Notkestr. 85, Hamburg 22607, Germany
*Corresponding author. E-mail: tkalcec@em.uni-frankfurt.de

(Received 30 July 2021; revision accepted 02 February 2022)

Abstract–Reliable identification of chondrules, calcium-aluminum-rich inclusions (CAIs), carbonate grains, and Ca-phosphate grains at depth within untouched, unprepared chondritic samples by a nondestructive analytical method, such as synchrotron X-ray fluorescence (SXRF) computed tomography (CT), is an essential first step before intrusive analytical and sample preparation methods are performed. The detection of a local Ca-enrichment could indicate the presence of such a component, all of which contain Ca as major element and/or Ca-bearing minerals, allowing it to be precisely located at depth within a sample. However, the depth limitation from which Ca-K fluorescence can travel through a chondrite sample (e.g., ~115 μm through material of 1.5 g cm^{-3}) to XRF detectors leaves many Ca-bearing components undetected at deeper depths. In comparison, Sr-K lines travel much greater distances (~1700 μm) through the same sample density and are, thus, detected from much greater depths. Here, we demonstrate a clear, positive, and preferential correlation between Ca and Sr and conclude that Sr-detection can be used as proxy for the presence of Ca (and, thus, Ca-bearing components) throughout mm-sized samples of carbonaceous chondritic material. This has valuable implications, especially for sample return missions from carbonaceous C-type asteroids, such as Ryugu or Bennu. Reliable localization, identification, and targeted analysis by SXRF of Ca-bearing chondrules, CAIs, and carbonates at depth within untouched, unprepared samples in the initial stages of a multianalysis investigation insures the valuable information they hold of pre- and post-accretion processes in the early solar system is neither corrupted nor destroyed in subsequent processing and analyses.

INTRODUCTION

Synchrotron X-ray fluorescence (SXRF) computed tomography (CT) is an ideal nonintrusive, nondestructive method to look into the interior of mm-sized objects and map the internal elemental distribution without the need for prior sample preparation in any form. This is particularly essential with extraterrestrial material, such as meteorites or asteroid material collected in sample return missions, due to the generally limited amount of material available and the consequential necessity for various analyses applying different investigative techniques to be performed on the same material. Even if a larger amount of material is available, valuable information can be missed if not located precisely before samples are cut, polished, or otherwise treated. The typically heterogeneous distribution and variable abundance and size of ancient components (e.g., calcium-aluminum-rich inclusions [CAIs], chondrules) in primitive solar system material, if present, makes their identification within the sample both challenging and essential before further sample processing. Exploratory 3-D analysis by noninvasive SXRF-CT is a useful tool to achieve this, determining the presence, general

distribution, and precise location of any such internal features within the primitive material. Furthermore, in sample return missions, the directly harvested material is delivered to Earth fully protected from the stresses and high temperatures involved with passage through the Earth's atmosphere to which meteorites are partly exposed. Initial analysis by SXRF can be performed with the pristine sample material still in air-free condition not having been exposed to terrestrial air, without risk of either contamination, corruption, or even destruction.

Carbonaceous chondrite material is generally considered to be the most primitive material in the solar system with chemical compositions, particularly those of CI chondrite material, closely approximating those of the bulk solar photosphere (McSween & Richardson, 1977). Attesting to the occurrence of hydration processes, the fine-grained matrices of the carbonaceous chondrites widely consist of phyllosilicates and other secondary minerals, such as high-Ca clinopyroxene, carbonates, iron sulfides, and iron oxides, typically produced by aqueous alteration (Scott & Krot, 2014). Carbonaceous chondrite meteorites are thought to originate from carbonaceous, C-type, asteroids, such as the target asteroids of sample return missions Hayabusa2 (JAXA) and OSIRIS-REx (NASA), returning dark carbonaceous chondritic material from the surface and subsurface layers of near-Earth asteroids (162173) Ryugu and (101955) Bennu, respectively (Lauretta et al., 2015; Watanabe et al., 2019). According to spectral data, the surface material of both Ryugu and Bennu is probably carbon-rich with widespread hydrated minerals and with strong similarities with the material of the aqueously altered CI and CM carbonaceous chondrites (Hamilton et al., 2019; Kitazato et al., 2019). For this reason, the Orgueil (CI) and Murchison (CM2) carbonaceous chondrites are suitable analogs, particularly for the asteroid material collected in the Hayabusa2 sample return mission, and can be analyzed for preparation and comparison purposes.

Optimal analysis of material brought to the Earth in sample return missions will involve a sequence of various analyses and analytical methods in a carefully scheduled order of performance. With its nondestructive ability to map interior elemental distributions, SXRF analysis is typically scheduled as one of the first in a sequence of many analyses to be performed on material from sample return missions. Time limitations and SXRF beam availabilities constrain the range of elements that can be analyzed reliably within a mm-sized sample of geological material and prioritization of the elements of most interest is essential for both diagnostic and technical reasons.

An important diagnostic element for the identification and localization of various components is calcium, present in a large range of primary and secondary phases typically found in samples of carbonaceous chondrite material. Chondrules and refractory inclusions, such as CAIs, contain primary and secondary Ca-bearing phases, including Ca-rich clinopyroxene, hibonite, perovskite, melilite, anorthite, grossular, hedenbergite, wollastonite, and monticellite, for example (Krot et al., 2021; MacPherson, 2007; MacPherson et al., 1984; Morrison & Hazen, 2020; Scott & Krot, 2007, 2014). Several carbonaceous chondrite classes (e.g., CM, CR2, CV3, and also CI) also contain frequent Ca-bearing carbonates (calcite, aragonite, and dolomite), sulfate (gypsum), and phosphate (apatite) in the form of individual grains or veins through the matrix (De Leuw et al., 2010; Lee & Nicholson, 2009; McSween & Richardson, 1977; Tomeoka & Buseck, 1988). While the CM class of carbonaceous chondrite is known to contain chondrules, CAIs, and also Ca-bearing carbonates and sulfates (Fendrich & Ebel, 2021; Hanowski & Brearley, 2001; Johnson & Prinz, 1993; King et al., 2017; McSween, 1979; Zolensky et al., 1997), the most primitive carbonaceous chondrite class, CI, is known to contain no chondrules nor CAIs but instead frequent Ca-bearing carbonates, mainly in the form of calcite and dolomite, and Ca-sulfates (De Leuw et al., 2010; Fredriksson & Kerridge, 1988; Lee & Nicholson, 2009). In contrast to, and as a likely consequence of, these Ca-rich components, the matrices of nearly all carbonaceous chondrites are systematically depleted in Ca relative to their respective bulk Ca concentrations (McSween & Richardson, 1977). Thus, any Ca-enriched areas detected in CI chondrite material are likely to consist of Ca-rich carbonates, phosphates, or sulfates.

Besides Ca, several other major elements, such as C, Mg, Al, Si, S, and Fe, could be also considered for the identification by SXRF of components such as chondrules, CAIs, and carbonates within chondritic material. Mg, Si, and Fe are typically very widespread in carbonaceous chondrite material, occurring in many minerals contained in CAIs, chondrules, and carbonates but are also the three main elements present within typical carbonaceous chondrite matrices, averaging $\sim$20, $\sim$32, and $\sim$38 wt%, respectively (McSween & Richardson, 1977). Furthermore, CI and CM chondrites have been reported to contain C up to 5 wt% (Gilmour, 2003), which could be an indication not only for carbonates, but also for organic material, the latter present as small patches dispersed throughout the matrix (Hayes, 1967; Tartèse et al., 2018). S occurs in pentlandite grains and pyrrhotite grains and has been identified in calcium sulfates in veins. Like Ca, the abundance of S in the matrix of carbonaceous chondrites is typically low, both averaging $\sim$2.5 wt% (McSween &

Richardson, 1977) but, unlike Ca, S does not play a significant role in CAI, chondrule, or carbonate minerals. The distributions of Mg, Ca, and Al are often used to efficiently define and distinguish the distributions of chondrules, CAIs, and carbonates (e.g., Krot, 2019; Scott & Krot, 2014). However, the distribution of Mg and Al is traditionally achieved by the application of more invasive analytic techniques (e.g., electron microscopy) that generally require more intrusive sample preparation and are, thus, more suitable for later stage investigations of material in sample return missions, rather than the initial investigations.

For optimal analysis of carbonaceous chondrite material, prioritization of the element or elements of most interest is essential not only for diagnostic considerations but also for technical reasons. Applying the noninvasive SXRF technique, internal elemental distribution maps of mm-sized particles are dependent upon the excitation and detection of the elements present, which is in turn controlled by the primary X-ray beam energy used in the SXRF analysis and the fluorescence line energies of the elements concerned. SXRF can practically be performed at beam energies between <5 and 100 keV, selected according to the elements of most interest and the technical specifications of the applicable beamline. Generally, low energy (<5 keV) X-ray radiation is able to excite with high efficiency and detect low-Z elements (Si-Ti), medium energy (10–20 keV) is able to excite with high efficiency and detect medium-Z elements as well as high-Z elements (the latter only by their L-lines), and high energy (70–100 keV) is able to excite with high efficiency and detect high-Z elements and rare earth elements by their Kα-lines but is less sensitive to low-Z elements. However, one of the main challenges in SXRF analysis of a mm-sized sample is, depending upon the type of bulk material involved, the detection of elements at deeper (>120 μm) levels within the sample. Excited by a primary (higher energy) photon that had successfully penetrated the sample volume depth to reach the element of interest, the fluorescent photon must then successfully travel through the volume of sample material to reach the external detectors. Particularly the detection of low-Z elements such as C, Mg, Al, Si, and S is hampered due to the limited penetration depth of their characteristic emission. For instance, in a CI matrix with a density of 1.5 g cm^{-3}, the penetration depths (i.e., the sample depth from which 99% of the photons are absorbed and only 1% of the photons can still escape the sample volume) of C, Mg, Al, Si, S, and Ca are 2.2, 12.1, 15.4, 22.8, 37.0, and 114.8 μm, respectively. It is clear that among these elements, Ca has by far the largest penetration depth and, relative to C, Mg, Al, Si, and S, can thus be potentially detected from the largest sample depth in a nondestructive fashion. However, the fluorescent Ca photons will fail to escape through depths greater than ~115 μm in a sample of 1.5 g cm^{-3} density and therefore remain undetected at the deeper levels, despite being detectable in regions toward the surface of the sample. This is the case for calcium (K_α: 3.692 keV), but not for strontium (K_α: 14.165 keV), which can travel ~1700 μm through material with a density of ~1.5 g cm^{-3} and, therefore, be detected throughout a mm-sized sample of carbonaceous chondrite material.

Thus, for the identification at depth of internal components such as chondrules, CAIs, and carbonates, calcium was selected as the most suitable element for both diagnostic and technical considerations. However, since the detection of Ca also has its depth limitations, we present here our findings to explore the validity of employing strontium as a proxy for the location of calcium at depth within carbonaceous chondrite material, such as CI and CM2 chondrites.

METHODS

SXRF measurements were performed at the Hard X-ray Micro/Nano-Probe beamline P06 end station of PETRA-III at DESY (Hamburg, Germany; Schroer et al., 2010). The undulator energy was set at 19.1 keV, rendered monochromatic by a PdB4C multilayer monochromator. The beam was focused by Kirkpatrick-Baez mirrors (JTEC, Japan) to approximately 1.2 × 0.7 μm^2 (V × H) at the sample position, with an approximate flux of 1.7 × 10e^{11} ph s^{-1}. XRF-CT measurements were performed in a 45° angle between the primary X-ray beam and detector chip normal axis, using a Vortex EM SDD detector with an 80 mm^2 sensitive area and 350 μm thick Si crystal, coupled to Xspress3 readout electronics. Additionally, a 5 mm diameter cylindrical collimator was combined with the XRF detector. With this setup, elements with atomic number (z) ranging $20 \leq z \leq 40$ were detected. XRF data were normalized for primary beam intensity fluctuations and detector dead time and were processed using PyMca v5.6.2 (Solé et al., 2007) fitting routines. XRF-CT scans were performed over a full 360° using an equidistant angular step size in the 0–180 and 180–360° ranges, where the latter range has an offset of half the step size compared with the 0–180° range in an interlaced sampling approach. XRF-CT reconstruction was performed using the TomoPy software package v1.9.1 (Gürsoy et al., 2014) using the gridrec reconstruction algorithm (Dowd et al., 1999).

SAMPLE

The CI carbonaceous chondrite Orgueil is reported to have a grain density of 2.42 g cm^{-3}, a porosity of $\sim$35%, and a bulk density of 1.58 g cm^{-3} (Macke et al., 2011). Its fine-grained, predominantly phyllosilicate matrix containing also magnetite, iron-sulfide, calcite, dolomite, ferrihydrite, and gypsum in decreasing order of abundance attests to it having undergone strong aqueous alteration and is the basis for its classification as petrologic type 1.1 (Bates et al., 2020; Endreß & Bischoff, 1993; Fredriksson & Kerridge, 1988; Gounelle & Zolensky, 2014; Kerridge, 1976; King et al., 2015; Lee & Nicholson, 2009; Tomeoka & Buseck, 1988). Phyllosilicates make up more than 84% of the Orgueil matrix (Bates et al., 2020; King et al., 2015, 2017) and consist of a mixture of Fe-bearing, Mg-rich serpentine and saponite (Tomeoka & Buseck, 1988). Also present in Orgueil are carbonate grains and veins, predominantly Ca-bearing and identified as calcite and dolomite (Lee & Nicholson, 2009) and calcium-sulfate veins. A sample piece of Orgueil, 252 × 240 × 276 μm in size, was placed on a thin carbon pad on an aluminum rod of 3 mm in diameter. No other sample preparation was performed prior to SXRF analysis.

RESULTS

An initial, depth-nonresolved, coarse overview SXRF scan was performed over the complete sample with a step size of 2 μm and an acquisition time of 0.75 s per pixel. The primary synchrotron beam (19.1 keV) penetrated the full sample depth and any Ca and Sr signals detected from the sample volume are projected depth-nonresolved onto the yz-plane (Fig. 1), revealing the full 2-D sample shape and Ca (a) and Sr (b) intensity distributions.

Although the detected Ca signals are of higher intensities than those of Sr, the Sr-rich regions detected by Sr-Kα signals are clearly more numerous. In the linearly scaled Ca and Sr distribution maps (Figs. 1c and 1d, respectively) the spatial coincidence of Ca and Sr is clearly evident (yellow circles) in many locations. Several Sr-rich spots toward the center of the sample do not have a Ca counterpart, including a $\sim$30 μm large Sr hotspot in the center (Fig. 1d). A tricolor RGB map (Fig. 1e) of the detected Fe (red), Ca (green), and Sr (blue) Kα-line signals clearly distinguishes between locations of joint Ca and Sr, depicted as light blue-green spots and located mainly in the peripheral regions, and locations of only Sr-detection, depicted in purple and predominantly toward the central regions. Although the yellow spots in the upper half of the sample suggest strong Ca-signals in joint location with Fe, the Sr-distribution map (Fig. 1d) confirms the additional presence of Sr at these locations, albeit at much lower intensities of $\sim$500 cts compared to the corresponding $\sim$2000 cts of Ca at these locations.

Three depth-resolved xy cross-section scans (CS1, CS3, CS2) were performed at three different heights of the *z*-axis of the sample, denoted in Fig. 1e, including one through the large Sr-hotspot (CS2), in order to determine the exact internal location of Ca-rich and Sr-rich features suggested by the depth-nonresolved coarse overview map (Fig. 1). During the depth-resolved tomographic cross-section scans, full sample rotation of 360° decreases the influence of self-absorption effects, thus increasing sensitivity toward features located farthest away from the detector. The 1-μm-thick tomographic cross-section slices CS1 and CS2 were acquired using a lateral step size of 1.5 μm, a rotation step size of 2°, and an acquisition time of 0.75 s per voxel. CS3 was acquired at higher resolution with a lateral step size of 1 μm, a rotation step size of 1°, and an acquisition time of 1 s per voxel. Fully depth-resolved Ca and Sr distribution maps of the three xy cross-section scans (Figs. 2a–c) confirm the spatial coincidence of detected Ca and Sr signals (Kα-lines) in the outer regions of the sample (Fig. 2, yellow circles) and the absence of detected Ca signals (Kα-lines) from the inner regions of the sample where only Sr Kα-lines are detected (Fig. 2, red arrows). It is interesting to note that the strong Sr signal of a large Sr-rich spot in CS2 (Fig. 2c, middle image) at around 80 μm depth beneath the sample surface has only a very weak suggestion of a corresponding Ca signal (Fig. 2c, left image). This only faintly perceivable Ca signal is nevertheless nonnegligible and cannot be dismissed, indicating the present but barely detectable Ca at the exact location of the strong Sr hotspot. This constrains a depth limitation of Ca signal detection in this particular chondritic material to $<\sim$80 μm. Tricolor RGB maps of the three cross section slices (Fig. 2 three right-hand images) showing detected Kα-line distributions of Fe (red), Ca (green), and Sr (blue) reconfirm in all three cross-section slices the detection of joint Sr and Ca signals (blue-green) in the outer surface or subsurface regions but the detection of only Sr signals (blue) in the inner depths of the sample.

In order to statistically quantify the correlation between Ca and Sr, Ca-correlation plots were calculated based on the intensities of detected Ca signals and those of the other eight most abundant elements, Ti, Cr, Mn, Fe, Co, Cu, Zn, and Sr, for each of the three cross-section slices (Fig. 3). In all three cross-section scans, the Ca-Sr correlation plot shows a clear and consistent, positive correlation, in stark contrast to the Ca-correlation plots with the other detected elements which

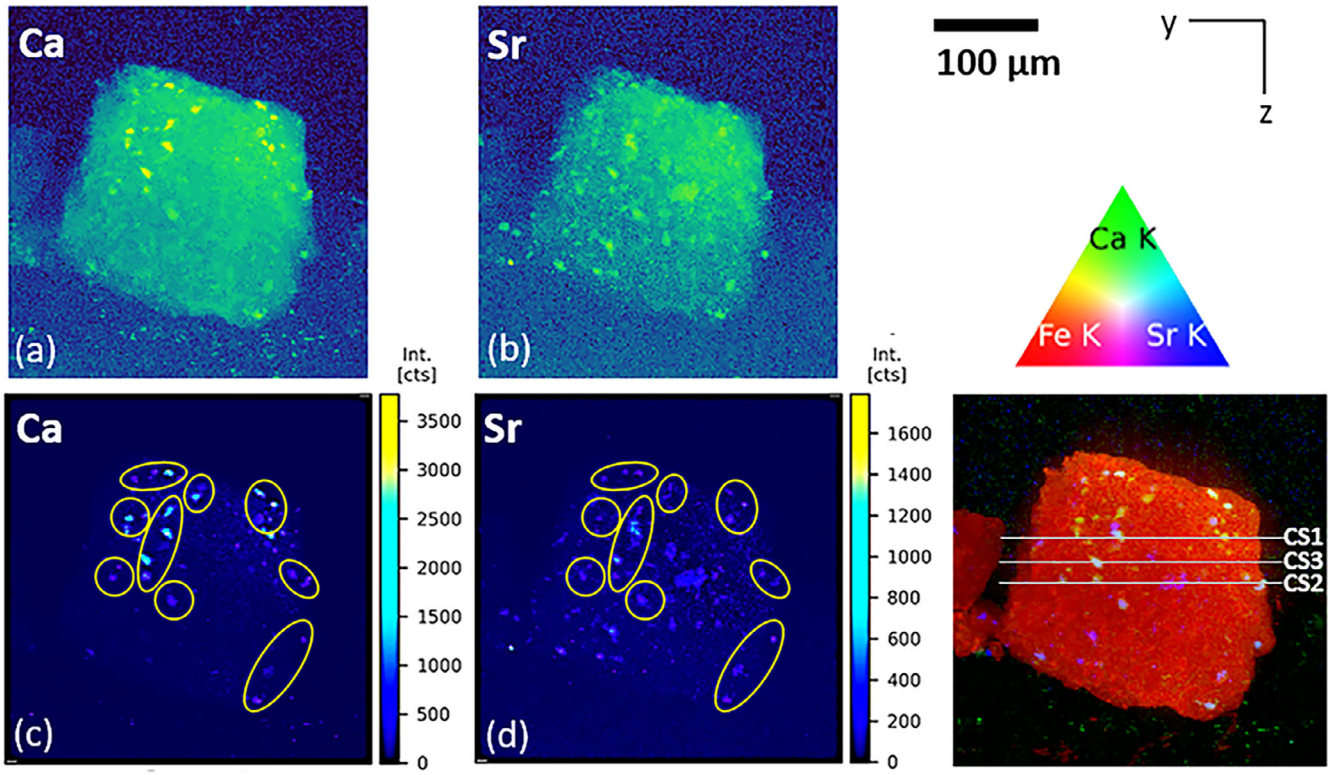

Fig. 1. Results of coarse overview SXRF scan of complete Orgueil sample. Detected Ca and Sr Kα-line signals projected depth-nonresolved from the 3-D volume onto the 2-D yz-plane. Log-scaled Ca (a) and Sr (b) intensity distributions reveal that detected Sr signals are more numerous relative to detected Ca signals. Linearly scaled Ca (c) and Sr (d) intensity distributions reveal frequent spatial coincidence of Ca and Sr (yellow circles). Further Sr-rich hotspots visible in inner regions have no Ca counterpart. RGB map (e) of detected Fe (red), Ca (green), and Sr (blue) visualizes the spatial coincidence of detected Ca and Sr. White solid lines in (e) denote the heights of three xy cross-section scans, one of which (CS2) was performed at the height of the large Sr-hotspot in the center of the Sr-intensity distribution image.

display either no Ca-correlation (Ti, Cr, Fe, Zn) or only weak and inconsistent correlations (Mn, Co, Cu). The Ca-Sr correlation plot for CS2 (Fig. 3) reveals a greater number of Sr-rich, Ca-poor data points compared to the Ca-Sr correlation plots of CS1 and CS3, which is likely associated with the large Sr-hotspot observed in both the Ca-K and RGB maps of CS2 (Fig. 2c middle and right, respectively).

In addition, Sr-correlation plots were also calculated based on the intensities of detected Sr signals and those of the other eight most abundant elements, including Ca, for each of the three cross-section slices (Fig. 4). In all three cross-section scans, the Sr-Ca correlation plot again shows a clear positive correlation, in stark contrast to the Sr-correlation plots with the other detected elements, which display either no Sr-correlation (Ti, Cr, Fe, Zn) or only weak and inconsistent correlations (Mn, Co, Cu).

The correlation strength, defined by the Pearson correlation coefficient (r), is numerically calculated for Ca- and Sr-correlations both with each other and also with the other seven most abundant elements detected in our three cross section scans (Table 1). The Pearson correlation coefficient results confirm clear Ca–Sr correlations in all three cross-section scans ($r = 0.46$, 0.76, 0.29) and only inconsistent, weak, negligible, or nonexistent correlations with the other elements: Ca and Sr weakly correlate with Mn ($0.11 < r < 0.19$); Sr correlates very weakly with Fe in a single cross-section (CS3; $r = 0.14$) and weakly with Co only in CS1 ($r = 0.18$); all other correlations are nonexistent or negligible ($0.00 < r < 0.07$). This numerical result confirms the visual observations, provided by the Ca and Sr distribution maps in Figs. 1 and 2, that a distinct and preferential correlation exists between Ca and Sr.

DISCUSSION

The considerable difference in concentration levels of a major element such as Ca and a trace element such as Sr does not affect the results of SXRF analysis. The high

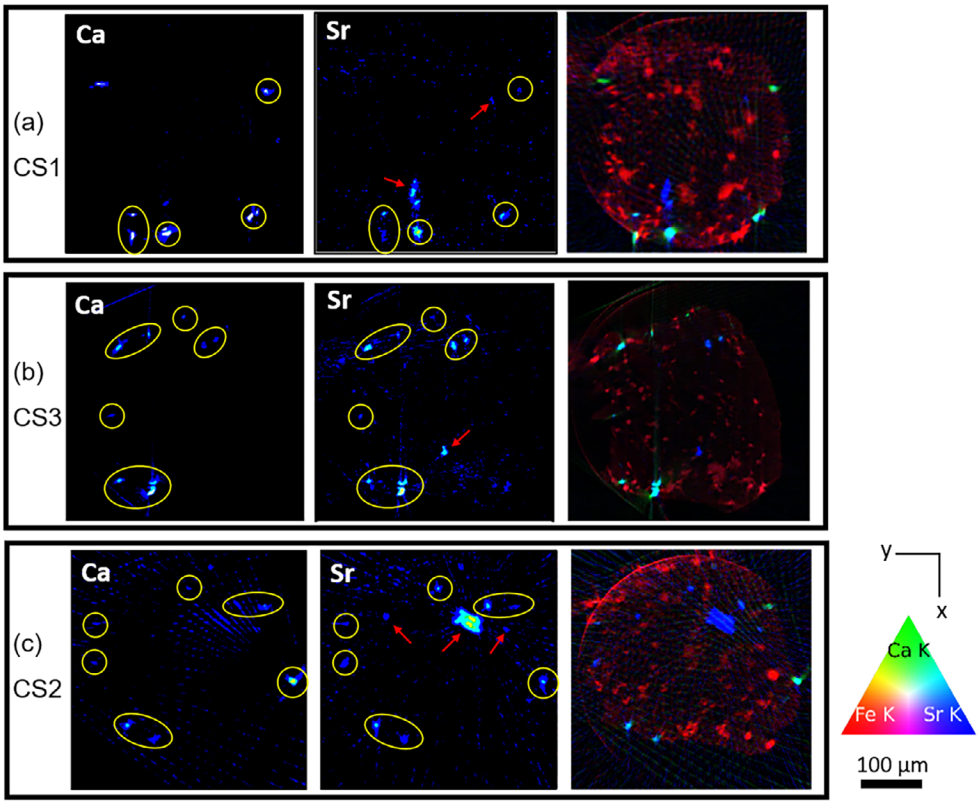

Fig. 2. Ca and Sr distribution maps of 1 µm thick xy cross-sections CS1 (a), CS3 (b), and CS2 (c) showing spatial coincidence of detected Ca and Sr Kα-line signals (yellow circles). In the three Sr maps, red arrows indicate the Sr signals that have no corresponding Ca signal. It is clearly noticeable that the red arrows are located in the more central areas of each map whereas the yellow circles (joint Ca-Sr signals) are located in the more peripheral areas, i.e., closer to the sample surface. The three maps on the right are tricolor (RGB) maps of FeCaSr distributions. The blue (Sr) dominance of the hotspots in the central areas compared to the blue-green (SrCa) hotspots toward the sample surface visualizes clearly that both Ca and Sr signals are detected from shallow depths but only the Sr signal is detected from deeper depths.

sensitivity of the SXRF analysis technique allows even low concentrations of trace elements, such as Sr, to be detected. With the SXRF equipment and detectors we used in this analysis, the detection limit for Sr in CI material is $\sim$7 ppm. Since each element is detected and recorded separately and the resulting element maps are individually scaled according to the count intensities acquired, the different concentrations of Ca and Sr in the Orgueil material examined play no role in the correlation results of this SXRF analysis. It is important to note that, despite its much lower concentration, the considerably higher atomic number of Sr (Z = 38) relative to that of Ca (Z = 20) allows information from Sr to travel a much greater distance (1.693 mm, see Fig. 5) compared to the 114.8 µm penetration depth of Ca in a material of 1.5 g cm^{-3} bulk density in order to escape the particle and reach the external detectors.

A clear and positive correlation of joint detections of Ca and Sr at the same location (voxel) is clearly shown in the Ca and Sr distributions in both the depth-nonresolved coarse yz-overview maps (Fig. 1) and the depth-resolved xy cross-section slices (Fig. 2). The xy cross-section slices further confirm that while both Ca and Sr are detected in the surface regions of the sample, only Sr is detected in the deeper levels. That the absence of detected Ca-signals in the central regions of the depth-nonresolved yz-overview scans could be an indication of the genuine absence of Ca in these regions is refuted by the strong Sr-hotspot in depth-resolved xy cross-section slice CS2 (Fig. 2c). Unlike the yz-coarse-overview scans, the 1 µm thickness and depth-resolved nature of the cross-section slices provide the exact position and depth in the selected slices (xy-planes) of any signals detected. The Sr-hotspot displayed in the center of the yz-image of the coarse overview scan (Figs. 1b, 1d, and 1e) is located in the cross-section slice CS2 at a depth of about 80 µm from the sample surface (Fig. 2c, middle). Thus, the extremely faint, barely visible, but nonetheless nonnegligible Ca

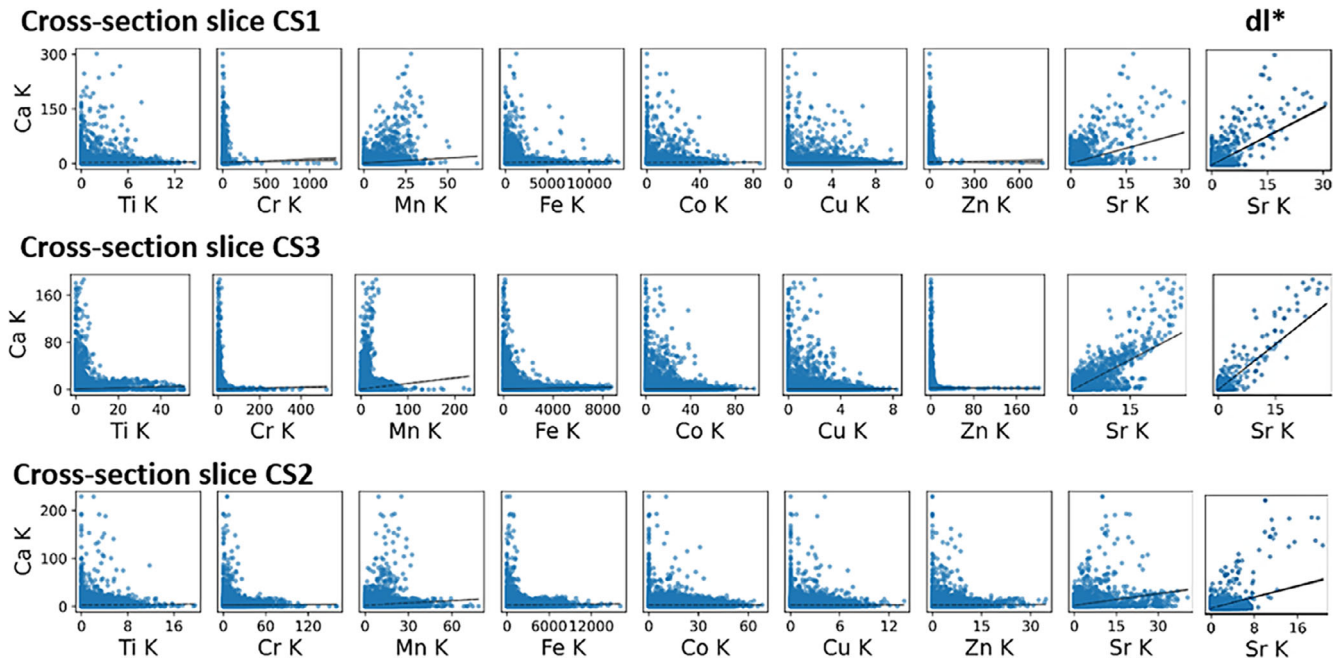

Fig. 3. Ca-correlation plots for the three cross-section slice scans performed on Orgueil based on the intensities of detected signals of Ca and those of the other eight most abundant elements detected, including Sr. dl* = depth-limited data subset that includes only data from near-surface regions, down to approx. 50 μm depth. Black lines are regression lines for visual orientation. N = 33,489, 90,000, and 33,489 data points for the full depth cross section slice plots of CS1, CS3, and CS2, respectively; N = 9052, 24,336, and 9052 data points for the depth-limited subset plots of CS1, CS3, and CS2, respectively. (Color figure can be viewed at wileyonlinelibrary.com.)

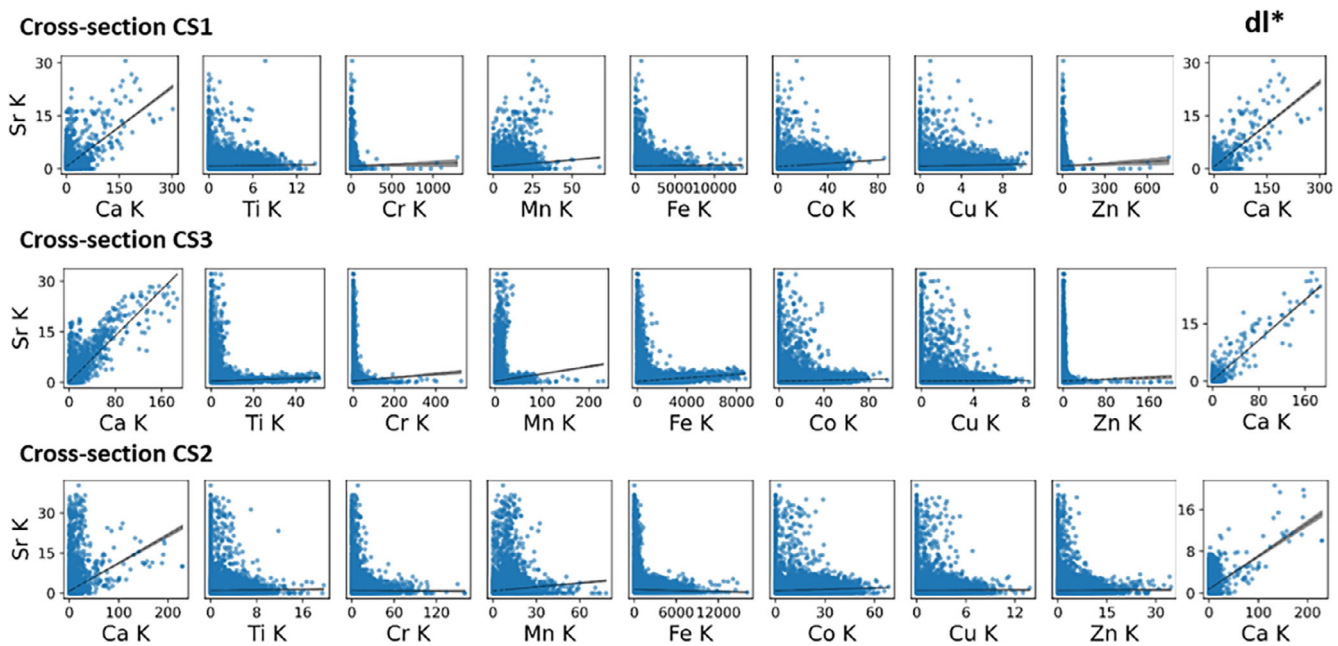

Fig. 4. Sr-correlation plots for the three cross-section slice scans performed on Orgueil based on the intensities of detected signals of Sr and those of the other eight most abundant elements detected, including Ca. dl* = depth-limited (includes only data from near-surface regions, down to approx. 50 μm depth). Black lines are regression lines for visual orientation. N = 33,489, 90,000, and 33,489 data points for the full depth cross-section slice plots of CS1, CS3, and CS2, respectively; N = 9052, 24,336, and 9052 for the depth-limited subset plots of CS1, CS3, and CS2, respectively. (Color figure can be viewed at wileyonlinelibrary.com.)

Table 1. Pearson correlation coefficient (r) between Ca and Sr and the seven next most abundant elements detected in Orgueil for each of the three cross-section slices.

		Ca	Ti	Cr	Mn	Fe	Co	Cu	Zn	Ca dl
CS1	Ca	–	0.02	0.02	0.19	0.03	0.01	0.01	0.00	–
	Sr	0.46	0.04	0.01	0.16	0.02	0.18	0.07	0.02	0.65
CS3	Ca	–	0.05	0.01	0.12	0.05	0.02	0.00	0.00	–
	Sr	0.76	0.05	0.04	0.11	0.14	0.06	0.02	0.02	0.70
CS2	Ca	–	0.03	0.01	0.14	0.03	0.00	0.00	0.02	–
	Sr	0.29	0.02	0.01	0.12	0.03	0.07	0.01	0.01	0.43

dl = depth-limited: only data from near-surface regions (down to approx. 50 μm depth) are included in the calculation.

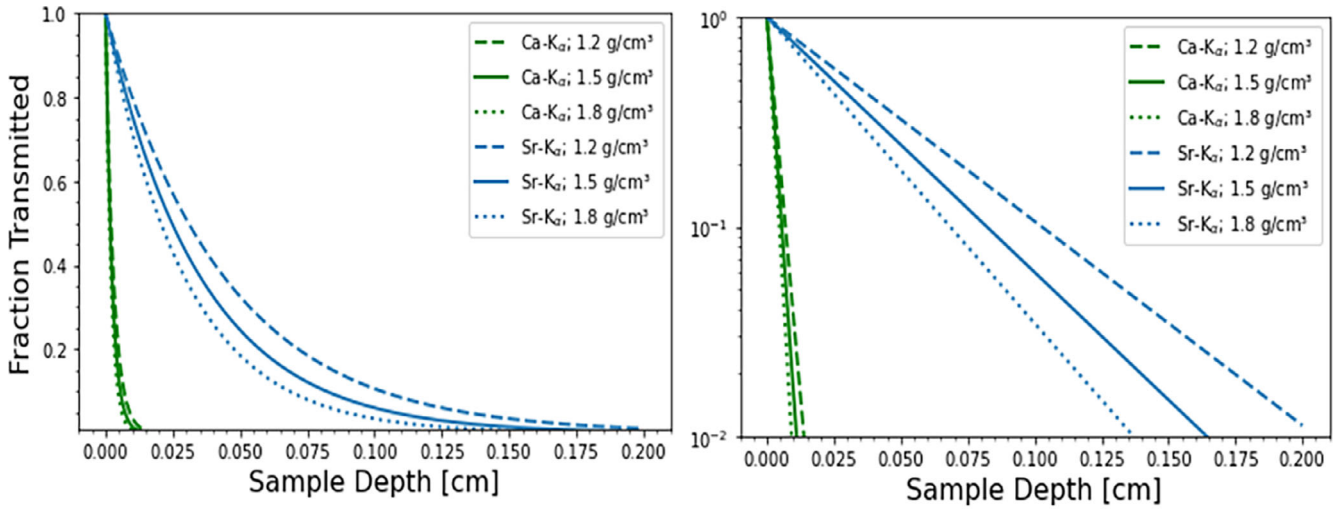

Fig. 5. Linear (left) and logarithmic (right) transmission fractions of Ca-Kα (green) and Sr-Kα (blue) as a function of their penetration depth through bulk material densities ranging from 1.20 to 1.80 g cm^{-3}.

signal in the same position (Fig. 2c, left) confirms that Ca is indeed present at this location but only faintly detectable, thus providing an approximate constraint for the maximum detection depth threshold for Ca signals in this carbonaceous chondrite at $<\sim 80$ μm. This is supported by the high-Sr/low-Ca data points (in the ranges $\sim 18<Sr<\sim 40$ and $0<Ca<\sim 35$) observed in the Ca-Sr correlation plot for CS2 but not for CS1 and CS3 (Fig. 3, second column from right) and likely attributable to the Sr-hotspot in CS2. Within this range, the Ca data points likely represent data acquired along the "northeastern" region of the Sr-hotspot (Fig. 2c, middle and right), i.e., the part of the Sr-hotspot that is closer to the sample surface and will, thus, show Sr-detection and some Ca-detection. The rest of the Sr-hotspot (i.e., extending deeper into the sample) will show Sr-detection but (increasingly less until) no Ca-detection. This supports the inference that the Sr-hotspot observed in CS2 straddles the threshold depth, below which Ca-detection in this material is not achieved.

The high correlation strength between Ca and Sr, revealed in the numerical Ca and Sr correlation plots (Figs. 3 and 4) of the cross-section slices CS1, CS3, and CS2 and their Pearson correlation coefficients (r) (Table 1), should be considered an underestimation of the real correlation strength. Since it is based on the detection of Sr and that of Ca, it will include any Sr detections at depth that have no Ca counterpart as a result of the much weaker energy of Ca fluorescent signals and their limited ability to travel through the same volume distances. These non-Ca-correlated Sr signals will negatively affect the Ca-Sr Pearson correlation coefficient (r) and, thus, the real Ca-Sr correlation strength is likely to be considerably greater.

For this purpose, a depth-limited (dl) subset of the full data set was additionally defined that includes only those data acquired within a rough depth limit of approximately 50 μm below the sample surface. A comparison of the Ca-Sr correlation plots from the full

sample data sets and the dl subsets (Fig. 3: two right-hand columns; and Fig. 4: first and last columns) for CS1, CS3, and CS2 reveal tighter and more clearly defined Ca-Sr correlations in the dl-subsets, relative to those of the full-sample plots. In all three cross-section slices, the high-Sr/low-Ca data points that are abundant in the full-sample data sets are absent in the dl-subsets, confirming that the high-Sr/low-Ca measurements were acquired at depths deeper than 50 μm. In particular, the absence of high-Sr/low-Ca data points in the CS2 dl correlation plots (Fig. 3 bottom right) reflects the absence of the Sr-hotspot (Fig. 2c middle and right) in the dl-subset. In addition, calculations of the Pearson correlation coefficient (r) were also made for the Ca-Sr correlation strengths of the dl-subsets of the three cross section slices (Table 1, far right column, and Table S1 in the supporting information). With r-values of 0.65 (CS1) and 0.43 (CS2), the Ca-Sr correlation results of the CS1 and CS2 dl-subsets are considerably stronger ($\sim$40 and $\sim$49%, respectively) than those of the full sample depths (r = 0.46 and 0.29, respectively). Although the r-value (0.70) for the CS3 dl-subset is slightly lower than that of the full sample data set (r = 0.76), which is likely a reflectance of sample heterogeneity at this particular z-height, both reflect a strong Ca-Sr Pearson correlation strength of over 0.70. Thus, we conclude that the Pearson correlation coefficient strengths, r = 0.65, 0.70, and 0.43, calculated for the Ca and Sr data acquired at depths limited to roughly 50 μm confirm the presence of a clear and convincing Ca-Sr correlation.

The correlation plots of both Ca and Sr with all other elements detected in this sample (shown for the full sample data sets in Figs. 3 and 4, respectively, and for the dl-data sets in Figs. S1–S3 in the supporting information) of cross-section slices CS1, CS3, and CS2, together with the numerical quantifications of their correlation strengths by the Pearson correlation coefficient (r) (Table 1 and Table S1) both demonstrate the preferentiality of the clear and consistent, positive Ca-Sr correlation, and only very weak, inconsistent, or nonexistent correlations between either Ca or Sr with any of the other main elements detected in the sample. The weak correlation of Mn with Ca and Sr in all cross-sections ($0.11 < r < 0.19$, Table 1) is not unexpected since both calcite and dolomite can contain Mn. However, the strongest Pearson correlation coefficient for Ca-Mn (r = 0.19 in CS1) is less than 66% of the weakest Ca-Sr correlation coefficient (r = 0.29 Ca-Sr in CS2) and a mere 25% of the strongest Ca-Sr correlation coefficient (r = 0.76 in CS3). Furthermore, unlike Sr that has a Kα energy of 14.165 keV, Mn-Kα energy is merely 5.900 keV and would therefore suffer much more absorption than Sr-Kα when traveling through the sample, resulting in a much shorter penetration depth (405.6 μm) of Mn compared to the 1693.2 μm penetration depth of Sr (through carbonaceous chondrite material with density of 1.5 g cm^{-3}). Thus, relative to Sr, the weaker Ca-Mn correlation and much shorter penetration depth of Mn renders Mn considerably less suitable than Sr to serve as proxy for Ca at depth.

In order to further assess the applicability, and consequential implications for sample return missions, such as Hayabusa2 and OSIRIS-REx, for using Sr as a proxy for the localization of Ca-bearing components, we considered the material density constraints involved. The bulk densities of Ryugu and Bennu have been determined as 1.19 ± 0.02 g cm^{-3} (Ryugu; Watanabe et al., 2019) and 1.19 ± 0.013 g cm^{-3} (Bennu; Scheeres et al., 2019). The average bulk densities of carbonaceous chondrites Orgueil (CI) and Murchison (CM2), the two carbonaceous chondrites thought to be most similar to Ryugu material, are reported as 1.58 and 2.3 g cm^{-3}, respectively (Macke et al., 2011). Thus, the above results of SXRF analysis of an Orgueil sample are based on penetration of a synchrotron beam, and passage of fluorescent (Kα-line) signals from the elements excited, through a sample with bulk material density of 1.58 g cm^{-3}. Our calculations show that penetration depths, defined as the distance at which 99% of the original photon flux is absorbed, of a synchrotron beam of 20 keV energy are 5.37 to 3.58 mm for bulk material densities ranging from 1.20 to 1.80 g cm^{-3}, respectively. Furthermore, our calculations show that for such bulk material densities (1.20–1.80 g cm^{-3}) the Sr- Kα- and Ca-Kα penetration depths range from 2.05 to 1.36 mm (Sr-Kα) and 0.14 to 0.01 mm (Ca-Kα) (Fig. 5).

This confirms that, for the bulk densities (of $\sim$1.19 g cm^{-3}) expected for carbonaceous chondrite material returned from C-type asteroids Ryugu and Bennu in sample return missions Hayabusa2 and OSIRIS-REx, the Sr-Kα fluorescent signals will be able to successfully travel through mm-sized samples to reach the external detectors, whereas the Ca-Kα signal will only be detectable from a maximum depth of $\sim$140 μm. This depth is greater than the approximated Ca-Kα detection depth constraint of $\sim$80 μm experimentally and visually inferred from our cross-section slice CS2 (Fig. 2c) and is likely a reflection of the higher average bulk density of Orgueil (1.58 g cm^{-3}) and the inhomogeneous nature of the material density of carbonaceous chondrites.

Ca-Affinity of Sr

The Ca-affinity of Sr is demonstrated in both primary condensation phases and secondary aqueous

alteration phases. Hibonite and perovskite, two early condensing, Ca-bearing refractory phases into which Sr is thought to directly condense from the solar nebula (Lodders, 2003) are two typical CAI minerals (Krot, 2019). In a hibonite-corundum inclusion in the CM2 meteorite Murchison, for example, Sr concentrations in three hibonite-dominated spots (two hibonite-corundum grains and one hibonite-perovskite-silicate grain) have been measured as 38.1–46 ppm (hib-cor) and 67.0 ppm (hib-pv-sil), with uncertainties <5% (Simon et al., 2002). The CI-normalized concentrations of Sr were calculated as ~5.5 (hib-cor) and ~9 (hib-pv-sil) (Simon et al., 2002). Secondary aqueous alteration phases, such as Ca-carbonates and Ca-sulfates, into which soluble Sr is transported and incorporated during aqueous alteration (Fredriksson & Kerridge, 1988; Jogo et al., 2018), are typically present in carbonaceous chondrites as grains or grain clusters (carbonates) and fibrous vein-fills (typically sulfates, less often carbonates; e.g., Fredriksson & Kerridge, 1988; Lee, 1993; McSween & Richardson, 1977). The concentrations of Sr in carbonate phases in CM and CI chondrites have been reported as up to 370 ± 2 ppm in CM calcite (Murchison; Riciputi et al., 1994), up to ~1900 ppm in CI aragonite (Orgueil; Fredriksson & Kerridge, 1988), up to 170 ± 5 ppm in CM dolomite (Nogoya), and up to 250 ± 4 ppm in CI dolomite (Orgueil; Riciputi et al., 1994). In comparison, slightly lower concentrations of Sr have been reported in natural terrestrial Ca-carbonate rocks of different ages with up to ~200 ppm pore-filling calcite cements (from Jurassic Smackover formations in Arkansas) and up to ~140 ppm dolomites (Mississipian Burlington-Keokuk; Banner, 1995). Interestingly, a clear correlation between Ca and Sr was reported in terrestrial Ca-carbonates as far back as 1971 (Veizer et al., 1971). In terrestrial calcium sulfates, Sr concentrations have been measured as 200 and 700 ppm (Cloutis et al., 2006).

Although the clear, positive Ca-Sr correlation demonstrated here in the CI carbonaceous chondrite Orgueil is likely attributed to the presence of Ca-rich carbonates and sulfates, this correlation has important implications for the analysis of chondrite material in general. By employing SXRF-CT analysis to determine the distribution of Sr-enriched spots or areas, the localization not only in surface regions but also at depth of Ca-bearing components, such as Ca-rich carbonate grains and veins, Ca-sulfate veins, CAIs, and Ca-bearing chondrules, is achieved without compromising the structural and chemical integrity of the sample. This is achieved with a two-step approach that also takes into consideration the time limitations generally involved in SXRF beamline access: an initial coarse overview scan of the complete mm-sized sample to show the depth-nonresolved Sr-distribution; and subsequent, depth-resolved, 1 μm thick, xy cross-section slices at *z*-heights defined by the positions of the more strongly detected Sr signals.

Terrestrial Weathering

Studies of ordinary chondrites found in the Oman desert have measured Sr concentrations up to 2200 ppm, which is 200 times higher than the Sr values of an unweathered ordinary chondrite, with isotopic oxygen studies concluding that the desert soils were the source of the excess Sr (Zurfluh et al., 2012). In these chondrites, terrestrially weathered in a hot desert environment, the high Sr concentrations are typically found in celestite ($SrSO_4$), a strontium-sulfate that often replaces gypsum. In the CI chondrite Orgueil, white sulfate veins have also been reported to be of terrestrial origin (Airieau et al., 2001; Gounelle & Zolensky, 2001), having formed from the reaction of terrestrial atmospheric water with the CI sulfate that remobilized and filled veins and pores in the brecciated, porous CI chondrite (Gounelle & Zolensky, 2001). It was concluded that specifically the highly friable and porous CI1 chondrites were most susceptible to the formation of sulfate veins through interaction with the terrestrial atmosphere. The sulfates present in Orgueil have been identified as Mg-sulfates and Ca-sulfates (Gounelle & Zolensky, 2001) and so far, no celestite has been reported in the literature in connection with Orgueil, or other CI carbonaceous chondrites, nor as resulting from interaction with the terrestrial atmosphere. However, a theoretical contemplation of the potential effects of any such terrestrial weathering on the Ca-Sr correlation results from our SXRF analysis of Orgueil would lead to two conclusions. First, that any presence of the strontium sulfate celestite with its high Sr concentration would have a weakening effect on a Ca-Sr correlation. Therefore, SXRF analysis of any carbonaceous chondrite that has undergone heavy terrestrial weathering in a hot desert environment would need to first rule out or identify the presence of celestite (based on extremely high Sr-concentrations in connection with S) before using the detection of Sr as proxy for a Ca-bearing phase. Second, the issue of hot desert terrestrial weathering will not be relevant for pristine carbonaceous chondrite material from sample return missions such as Hayabusa2 or OSIRIS-REx for which the use of Sr as a proxy for Ca distribution is particularly useful.

CONCLUSIONS

We have demonstrated that there is a clear and preferential positive correlation between Sr and Ca in the carbonaceous CI chondrite Orgueil, which can be

applied to other carbonaceous chondritic material, such as CM material. This Ca-Sr correlation allows the internal distribution of Ca-rich components, such as calcium-carbonate grains and veins and calcium-sulfate veins, as well as CAIs and calcium-bearing chondrules, in mm-sized samples to be determined by SXRF spectroscopy in a nonintrusive, nondestructive, noncompromising analysis with a two-step approach that involves first a depth-nonresolved coarse yz-overview map of the complete sample, followed by depth-resolved xy-cross section slice maps strategically selected at the *z*-heights corresponding to Sr-rich spots identified in the coarse overview map. This Sr-Ca correlation and two-step analysis approach is particularly suitable for the initial analysis of unique and pristine material collected from primitive carbonaceous C-type asteroids, such as Ryugu and Bennu, in sample return missions such as Hayabusa2 and OSIRIS-REx.

Acknowledgments—We are grateful for financial support provided by the Dr. Rolf M. Schwiete Stiftung and the DFG (grant BR2015/38-1) (B.J.T.). P.T. would like to thank BOF (grant BOF20/PDO/037) and FWO (grant 12Q7718N) for financial support. This research was supported in part by the special research fund of Ghent University under project number BOF17-GOA-015 (B.V.) and by the FWO Research Projects G0D5221N and G099817N. We acknowledge DESY (Hamburg, Germany), a member of the Helmholtz Association HGF, for the provision of experimental facilities. Parts of this research were carried out at PETRA III and we would like to thank the P06 staff for their assistance. Beamtime was allocated for proposal II-20190012 EC. The research leading to this result has been supported by the project CALIPSOplus under the Grant Agreement 730872 from the EU Framework Programme for Research and Innovation HORIZON 2020. Open access funding enabled and organized by Projekt DEAL. This work was supported by JSPS KAKENHI Grant Number 20H00188 to TN.

Data Availability Statement—The data that support the findings of this study are available from the corresponding author upon reasonable request.

Editorial Handling—Edward Cloutis

REFERENCES

Airieau, S. A., Farquhar, J., Jackson, T. L., Leshin, L. A., Thiemens, M. H., and Bao, H. 2001. Oxygen Isotope Systematics of CI and CM Chondrite Sulfate: Implications for Evolution and Mobility of Water in Planetesimals (Abstract #1744). 32nd Lunar and Planetary Science Conference. CD-ROM.

Banner, J. L. 1995. Application of the Trace Element and Isotope Geochemistry of Strontium to Studies of Carbonate Diagenesis. *Sedimentology* 42: 805–24.

Bates, H. C., King, A. J., Donaldson Hanna, K. L., Bowles, N. E., and Russell, S. S. 2020. Linking Mineralogy and Spectroscopy of Highly Aqueously Altered CM and CI Carbonaceous Chondrites in Preparation for Primitive Asteroid Sample Return. *Meteoritics & Planetary Science* 55: 77–101.

Cloutis, E. A., Hawthorne, F. C., Mertzman, S. A., and Krenn, K. 2006. Detection and Discrimination of Sulfate Minerals Using Reflectance Spectroscopy. *Icarus* 184: 121–157.

De Leuw, S., Rubin, A. E., and Wasson, J. T. 2010. Carbonates in CM Chondrites: Complex Formational Histories and Comparison to Carbonates in CI Chondrites. *Meteoritics & Planetary Science* 45: 513–30.

Dowd, B. A., Campbell, G. H., Marr, R. B., Nagarkar, V. V., Tipnis, S. V., Axe, L., and Siddons, D. P. 1999. Developments in Synchrotron X-Ray Computed Microtomography at the National Synchrotron Light Source. *Developments in X-Ray Tomography II* 3772: 224–36.

Endreß, M., and Bischoff, A. 1993. Mineralogy, Degree of Brecciation and Aqueous Alteration of CI Chondrites Orgueil, Ivuna, and Alais. *Meteoritics* 28: 345–6.

Fendrich, K. V., and Ebel, D. S. 2021. Comparison of the Murchison CM2 and Allende CV3 Chondrites. *Meteoritics & Planetary Science* 56: 77–95.

Fredriksson, K., and Kerridge, J. F. 1988. Carbonates and Sulfates in CI Chondrites: Formation by Aqueous Activity on the Parent Body. *Meteoritics* 23: 35–44.

Gilmour, I. 2003. Structural and Isotopic Analysis of Organic Matter in Carbonaceous Chondrites. In *Treatise on Geochemistry*, edited by A. M. Davis, H. D. Holland, and K. K. Turekian, 269–90. Oxford: Elsevier Ltd.

Gounelle, M., and Zolensky, M. E. 2001. A Terrestrial Origin for Sulfate Veins in CI1 Chondrites. *Meteoritics & Planetary Science* 36: 1321–9.

Gounelle, M., and Zolensky, M. E. 2014. The Orgueil Meteorite: 150 Years of History. *Meteoritics & Planetary Science* 49: 1769–94.

Gürsoy, D., De Carlo, F., Xiao, X., and Jacobsen, C. 2014. TomoPy: A Framework for the Analysis of Synchrotron Tomographic Data. *Journal of Synchrotron Radiation* 21: 1188–93.

Hamilton, V. E., Simon, A. A., Christensen, P. R., Reuter, D. C., Clark, B. E., Barucci, M. A., Bowles, N. E. et al. 2019. Evidence for Widespread Hydrated Minerals on Asteroid (101955) Bennu. *Nature Astronomy* 3: 332–40.

Hanowski, N. P., and Brearley, A. J. 2001. Aqueous Alternation of the Chondrules in the CM Carbonaceous Chondrite, Alla Hills 81002: Implications for Parent Body Alternation. *Geochimica et Cosmochimica Acta* 65: 495–518.

Hayes, J. M. 1967. Organic Constituents of Meteorites—A Review. *Geochimica et Cosmochimica Acta* 31: 1395–440.

Jogo, K., Ito, M., Nakamura, T., Kobayashi, S., and Lee, J. I. 2018. Redistribution of Sr and Rare Earth Elements in the Matrices of CV3 Carbonaceous Chondrites During Aqueous Alteration in Their Parent Body. *Earth, Planets and Space* 70: 37. https://doi.org/10.1186/s40623-018-0809-5

Johnson, C. A., and Prinz, M. 1993. Carbonate Compositions in CM and CI Chondrites and Implications for Aqueous Alteration. *Geochimica et Cosmochimica Acta* 57: 2843–52.

Kerridge, J. F. 1976. Major Element Composition of Phyllosilicates in the Orgueil Carbonaceous Meteorite. *Earth and Planetary Science Letters* 29: 194–200.

King, A. J., Schofield, P. F., and Russell, S. S. 2017. Type 1 Aqueous Alteration in CM Carbonaceous Chondrites: Implications for the Evolution of Water-Rich Asteroids. *Meteoritics & Planetary Science* 52: 1197–215.

King, A. J., Solomon, J. R., Schofield, P. F., and Russell, S. S. 2015. Characterising the CI and CI-Like Carbonaceous Chondrites Using Thermogravimetric Analysis and Infrared Spectroscopy Planetary Science. *Earth, Planets and Space* 67: 198. https://doi.org/10.1186/s40623-015-0370-4

Kitazato, K., Milliken, R. E., Iwata, T., Abe, M., Ohtake, M., Matsuura, S., Arai, T. et al. 2019. The Surface Composition of Asteroid 162173 Ryugu from Hayabusa2 Near-Infrared Spectroscopy. *Science* 364: 272–5.

Krot, A. N. 2019. Refractory Inclusions in Carbonaceous Chondrites: Records of Early Solar System Processes. *Meteoritics & Planetary Science* 54: 1647–91.

Krot, A. N., Petaev, M. I., and Nagashima, K. 2021. Infiltration Metasomatism of the Allende Coarse-Grained Calcium-Aluminum-Rich Inclusions. *Progress in Earth and Planetary Science* 4: 61.

Lauretta, D. S., Bartels, A. E., Barucci, M. A., Bierhaus, E. B., Binzel, R. P., Bottke, W. F., Campins, H. et al. 2015. The OSIRIS-REx Target Asteroid (101955) Bennu: Constraints on Its Physical, Geological, and Dynamical Nature from Astronomical Observations. *Meteoritics & Planetary Science* 50: 834–49.

Lee, M. R. 1993. The Petrography, Mineralogy and Origins of Calcium Sulphate Within the Cold Bokkeveld CM Carbonaceous Chondrite. *Meteoritics* 28: 53–62.

Lee, M. R., and Nicholson, K. 2009. Ca-Carbonate in the Orgueil (CI) Carbonaceous Chondrite: Mineralogy, Microstructure and Implications for Parent Body History. *Earth and Planetary Science Letters* 280: 268–75.

Lodders, K. 2003. Solar System Abundances and Condensation Temperatures of the Elements. *The Astrophysical Journal* 591: 1220.

Macke, R. J., Consolmagno, G. J., and Britt, D. T. 2011. Density, Porosity, and Magnetic Susceptibility of Carbonaceous Chondrites. *Meteoritics & Planetary Science* 46: 1842–62.

Macpherson, G. J. 2007. Calcium-Aluminium-Rich Inclusions in Chondritic Meteorites. In *Treatise on Geochemistry*. Meteorites, Planets, and Comets, edited by A. M. Davis, H. D. Holland, and K. K. Turekian, 1–47. Oxford: Elsevier Ltd.

MacPherson, G. J., Grossman, L., Hashimoto, A., Bar-Matthews, M., and Tanaka, T. 1984. Petrographic Studies of Refractory Inclusions from the Murchison Meteorite. *Journal of Geophysical Research* 89: C299.

McSween Jr., H. Y. 1979. Alteration in CM Carbonaceous Chondrites Inferred from Modal and Chemical Variations in Matrix. *Geochimica et Cosmochimica Acta* 43: 1761–70.

McSween, H. Y., and Richardson, S. M. 1977. The Composition of Carbonaceous Chondrite Matrix. *Geochimica et Cosmochimica Acta* 41: 1145–61.

Morrison, S. M., and Hazen, R. M. 2020. An Evolutionary System of Mineralogy. Part II: Interstellar and Solar Nebula Primary Condensation Mineralogy (>4.565 Ga). *American Mineralogist* 105: 1508–35.

Riciputi, L. R., McSween Jr., H. Y., Johnson, C. A., and Prinz, M. 1994. Minor and Trace Element Concentrations in Carbonates of Carbonaceous Chondrites, and Implications for the Compositions of Coexisting Fluids. *Geochimica et Cosmochimica Acta* 58: 1343–51.

Scheeres, D. J., McMahon, J. W., French, A. S., Brack, D. N., Chesley, S. R., Farnocchia, D., Takahashi, Y. et al. 2019. The Dynamic Geophysical Environment of (101955) Bennu Based on OSIRIS-REx Measurements. *Nature Astronomy* 3: 352–61.

Schroer, C. G., Boye, P., Feldkamp, J. M., Patommel, J., Samberg, D., Schropp, A., Schwab, A. et al. 2010. Hard X-Ray Nanoprobe at Beamline P06 at PETRA III. *Nuclear Instruments and Methods in Physics Research, Section A: Accelerators, Spectrometers, Detectors and Associated Equipment* 616: 93–7.

Scott, E. R. D., and Krot, A. N. 2007. Chondrites and Their Components. In *Treatise on Geochemistry*, edited by H. D. Holland, and K. K. Turekian. Oxford: Elsevier Pergamon. vol. 1, pp. 1–72.

Scott, E. R. D. and Krot, A. N. 2014. Meteorites and Cosmochemical Processes. In *Chondrites and Their Components*, Treatise on Geochemistry, edited by H. D. Holland, and K. K. Turekian, 2nd ed, 65–137. Oxford: Elsevier Ltd.

Simon, S. B., Davis, A. M., Grossman, L., and Keegan, K. D. M. C. 2002. A Hibonite-Corundum Inclusion from Murchison: A First-Generation Condensate from the Solar Nebula. *Meteoritics & Planetary Science* 37: 533–48.

Solé, V. A., Papillon, E., Cotte, M., Walter, P., and Susini, J. 2007. A Multiplatform Code for the Analysis of Energy-Dispersive X-Ray Fluorescence Spectra. *Spectrochimica Acta—Part B Atomic Spectroscopy* 62: 63–8.

Tartèse, R., Chaussidon, M., Gurenko, A., Delarue, F., and Robert, F. 2018. Insights into the Origin of Carbonaceous Chondrite Organics from Their Triple Oxygen Isotope Composition. *Proceedings of the National Academy of Sciences* 115: 8535–40.

Tomeoka, K., and Buseck, P. R. 1988. Matrix Mineralogy of the Orgueil CI Carbonaceous Chondrite. *Geochimica et Cosmochimica Acta* 52: 1627–40.

Veizer, J., Demovic, R., and Turan, J. 1971. Possible Use of Strontium in Sedimentary Carbonate Rocks as a Paleoenvironmental Indicator. *Sedimentary Geology* 5: 5–22.

Watanabe, S., Hirabayashi, M., Hirata, N., Hirata, N. A., Noguchi, R., Shimaki, Y., Ikeda, H. et al. 2019. Hayabusa2 Arrives at the Carbonaceous Asteroid 162173 Ryugu—A Spinning Top-Shaped Rubble Pile. *Science* 364: 268–72.

Zolensky, M. E., Mittlefehldt, D. W., Lipschutz, M. E., Wang, M. S., Clayton, R. N., Mayeda, T. K., Grady, M. M., Pillinger, C., and Barber, D. 1997. CM Chondrites Exhibit the Complete Petrologic Range from Type 2 to 1. *Geochimica et Cosmochimica Acta* 61: 5099–115.

Zurfluh, F. J., Hofmann, B., Gnos, E., Eggenberger, U., Greber, N. D., and Villa, I. M. 2012. Weathering and Strontium Contamination of Meteorites Recovered in the Sultanate of Oman. *Meteorite* 18: 34–8.

SUPPORTING INFORMATION

Additional supporting information may be found in the online version of this article.

Fig. S1. Correlation plots for the dl-subset for cross section slice scan CS1 based on the intensities of detected signals of Ca and Sr and those of the other seven most abundant elements detected. The depth-limited subset includes only data from near-surface regions (down to approx. 50 μm depth). $N = 9052$ data points.

Fig. S2. Correlation plots for the dl-subset for cross section slice scan CS3 based on the intensities of detected signals of Ca and Sr and those of the other seven most abundant elements detected. The depth-limited subset includes only data from near-surface regions (down to approx. 50 μm depth). $N = 24{,}336$ data points.

Fig. S3. Correlation plots for the dl-subset for cross section slice scan CS2 based on the intensities of detected signals of Ca and Sr and those of the other seven most abundant elements detected. The depth-limited subset includes only data from near-surface regions (down to approx. 50 μm depth). $N = 9052$ data points.

Table S1. Pearson correlation coefficient (r) between Ca and Sr and the seven next most abundant elements detected in Orgueil for the dl-data subset for each of the three cross section slices. *dl = depth-limited subset includes only data from near-surface regions (down to approx. 50 μm depth).